Long pulse FRC sustainment with enhanced edge driven rotating magnetic field current drive

2005 Nucl. Fusion 45 176

(http://iopscience.iop.org/0029-5515/45/3/003)

INSTITUTE OF PHYSICS PUBLISHING and INTERNATIONAL ATOMIC ENERGY AGENCY NUCLEAR FUSION

Nucl. Fusion **45** (2005) 176–183 doi:10.1088/0029-5515/45/3/003

Long pulse FRC sustainment with enhanced edge driven rotating magnetic field current drive

A.L. Hoffman[a], **H.Y. Guo, K.E. Miller and R.D. Milroy**

Redmond Plasma Physics Laboratory, University of Washington, Seattle, WA, USA

E-mail: hoffman@aa.washington.edu

Received 17 November 2004, accepted for publication 27 January 2005
Published 21 February 2005
Online at stacks.iop.org/NF/45/176

Abstract

Field reversed configurations (FRCs) have been formed and sustained for up to 50 normal flux decay times by rotating magnetic fields (RMFs) in the translation, confinement, and sustainment experiment. For these longer pulse times a new phenomenon has been observed: switching to a higher performance mode delineated by shallower RMF penetration, higher ratios of generated poloidal to RMF drive field, and lower overall plasma resistivity. This mode switching is always accompanied by, and perhaps triggered by, the spontaneous development of a toroidal field with a magnitude up to 20% of the peak poloidal field. The global data cannot be explained by previous RMF theory based on uniform electron rotational velocities or by numerical calculations based on uniform plasma resistivity, but agrees in many respects with new calculations made using strongly varying resistivity profiles. In order to more realistically model RMF driven FRCs with such non-uniform resistivity profiles, a double rigid rotor model has been developed with separate inner and outer electron rotational velocities and resistivities. The results of this modelling suggest that the RMF drive results in very high resistivity in a narrow edge layer, and that the higher performance mode is characterized by a sharp reduction in resistivity over the bulk of the FRC.

PACS numbers: 52.55Lf

(Some figures in this article are in colour only in the electronic version)

1. Introduction

Field reversed configurations (FRCs) differ from all other toroidal plasmas, such as tokamaks, reversed field pinches, and spheromaks, in that they have minimal toroidal field and their toroidal current is thus almost purely diamagnetic. That current is then simply the manifestation of a pressure gradient. Sustaining or growing the configuration amounts to sustaining or increasing the poloidal flux (and hence the pressure gradient), which requires maintaining the toroidal electric field at or above zero. The use of rotating magnetic fields (RMFs) to accomplish this has a long history, primarily in rotamak devices [1]. In the absence of heating or fuelling near the field null, a simple approximate expression has been derived for the rate of change of poloidal flux for elongated (prolate) FRCs:

$$\frac{\mathrm{d}\phi_p}{\mathrm{d}t} = 2\pi R E_\theta(R) = \frac{2}{n_\mathrm{e} e R^2 l_\mathrm{s}}(T_\mathrm{RMF} - T_\eta), \qquad (1)$$

where r_s is the separatrix radius, $R = r_\mathrm{s}/\sqrt{2}$ the radius of the field null for an elongated FRC, n_e the electron density, l_s the FRC separatrix length, and T_RMF and T_η are the torques produced by the RMF and by electron–ion friction (resistivity) [2].

The cross-field plasma resistivity is a key confinement parameter since minimizing the resistivity will minimize the required external torque, and thus the power required to maintain the configuration. In our experiments the RMF is applied to a weakly pre-ionized deuterium gas inside a flux conserver of radius r_c in the presence of an axial bias field B_0. As an FRC is formed and its poloidal flux built up, r_s increases, compressing the external flux, $\phi_\mathrm{e} = \pi r_\mathrm{c}^2 B_0$, and raising the external field to $B_\mathrm{e} = B_0/(1 - x_\mathrm{s}^2)$, where $x_\mathrm{s} \equiv r_\mathrm{s}/r_\mathrm{c}$. This results in an increasing resistive torque, and a quasi-steady condition is reached when T_η equals T_RMF.

Most RMF analyses have been based on assuming a uniform plasma resistivity and a uniform electron rotational frequency ω_e (rigid rotor (RR) model) at some fraction $\omega_\mathrm{e} = \zeta\omega$ of the RMF frequency ω [2–4]. (Our formal definition of ζ for an elongated FRC is $\zeta = I'/I'_\mathrm{synch}$ where $I' = (B_z(r_\mathrm{s}) - B_z(0))/\mu_0$ is the diamagnetic line current and $I'_\mathrm{synch} = 0.5\langle n_\mathrm{e}\rangle e\omega r_\mathrm{s}^2$ is the maximum possible line current synchronous with the RMF, assuming the ion rotational

[a] Author to whom any correspondence should be addressed.

frequency $\omega_i = 0$.) For a given RMF amplitude, B_ω, this analysis produces a relationship between the applied RMF torque, the plasma resistivity, and the achievable plasma density [5, 6]. However, experimentally, when the resistivity was estimated based on the ratio of absorbed RMF power to the square of the driven current, serious discrepancies were noted. Much higher plasma densities and driven currents were produced than calculated, especially when taking into account FRC lengths l_s greater than the RMF antenna length l_a [7]. Under some low ζ drive conditions experimental features were also observed that could not be accounted for by simple uniform resistivity modelling; most notably the RMF not penetrating to the FRC magnetic field null. These features are prominent in the measurements reported here. Although we have always modelled RMF drive in terms of total RMF and resistive torques, assuming that radial plasma flow could redistribute the RMF drive forces, it was difficult to understand how the FRC flux could be maintained with so little RMF drive at the null, where the RMF flow driven *EMF*, $v_r \times B_z$, was unavailable.

The significance of the RMF penetration profile has become more apparent in recent experiments on the translation, confinement, & sustainment (TCS) device [8], where the discharge pulse lengths were extended from 2.5 to 10 ms by increasing the size of the RMF capacitor bank from 30 to 60 kJ. It was then observed that the performance, as indicated by spontaneous switching between different ratios of the external confinement field B_e to B_ω, would undergo abrupt changes. This was accompanied by subtle but highly repeatable switches in the RMF profile $B_\theta(r)$ between shallower penetration (higher performance) and deeper penetration (lower performance). Recent calculations with non-uniform resistivities, which illuminate the 'edge driven' process [9], provide a mechanism for understanding this phenomenon, and lead to simple methods for evaluating the resistivity differences between the two modes. The plasma must have high resistivity in the driven, low density edge region, but much lower resistivity throughout the bulk of the FRC. Many features, such as a non-steady behaviour with cyclical RMF tearing and reconnection caused by vastly different edge and central electron rotational speeds, which are predicted by the non-uniform resistivity calculations, are seen in the experimental measurements [9].

Switching to the higher performance mode was always accompanied by, and sometimes preceded by, the development of the toroidal field. This toroidal field was concentrated near the field null with a magnitude of 10–20% of the peak poloidal field, and thus did not significantly affect the high-β nature of the FRC equilibrium. ($\langle\beta\rangle = 1 - 0.5x_s^2$ is a consequence of axial equilibrium for elongated FRCs confined inside cylindrical flux conservers.) It has been noted in previous rotamak experiments that significantly higher performance (tripling of the achievable toroidal current) could be attained when an external toroidal field was imposed using a central current carrying rod, but in those cases the toroidal field near the field null exceeded the peak poloidal field, and the magnetic configuration was that of an spherical tokamak (ST) [10]. Those recent results were also somewhat in contradiction to earlier RMF driven ST experiments where the toroidal field addition had very minor benefits [11]. We, thus, cannot say

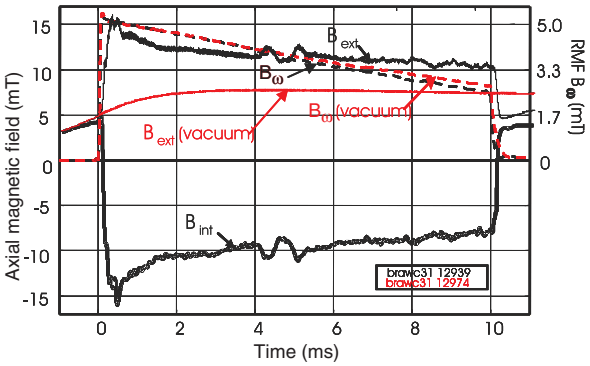

Figure 1. Long pulse operation of TCS. B_{int} and B_{ext} are obtained from internal probes located at $r = 0$ and 40 cm.

definitively whether our spontaneous toroidal field generation has any bearing on the improved performance that we observe, but it certainly is an interesting phenomenon.

In order to analyse the mode switching in the simplest possible analytical manner, we develop a double RR (DRR) extension to the previous uniform resistivity simple RR analysis. The bulk of the FRC electrons are assumed to be rotating at a velocity determined from the measured density and total diamagnetic current, while a narrow edge layer is assumed to co-rotate with the RMF. The central rotation speed and position of the edge layer are determined from simple equilibrium considerations. Separate resistivities in each portion are calculated by matching the total resistive torque to the RMF drive torque, and the Ohmic power absorption in both portions to the total measured deposited RMF power. In this manner, it is calculated that the switching to high performance mode signifies a sharp reduction in the central resistivity. Since the toroidal field is so small compared to the peak poloidal field, it does not enter into the analysis and, while it may be expected that the relatively large ratios of toroidal field to poloidal field near the field null may have effects on nominal 'cross-field' resistivity, this topic is not a focal point of this paper.

2. Basic experimental operation

TCS has a 2.6 m long, 80 cm internal diameter vacuum chamber consisting of two 1.25 m long quartz tubes joined by a metal foil lined plastic ring containing vacuum access ports. Various measurements, such as internal magnetic field probing, CO_2 interferometry, and bolometry are performed through these access ports. An axial bias field is provided by a parallel arrangement of (20) 56-turn coils at an effective flux confining radius of 47 cm. The coils are powered by a small capacitor bank with a rise time of about 4 ms, and then crowbarred. There are also azimuthal copper straps (flux rings) placed directly on the vacuum vessel, with effective L/R field penetration times (in vacuum) of ~4 ms. When the RMF is activated in the presence of a slightly pre-ionized D_2 gas fill and initial axial bias field, an FRC is rapidly formed, compressing the external flux against the flux confining boundaries, and raising the external field. The basic experimental operation is indicated by the time traces of external and internal magnetic fields, and the traces of B_ω (always derived from the measured RMF antenna currents), shown in figure 1. The FRC internal field

has approximately the same magnitude as the external field, which is typical of RMF driven FRCs. The operation is very insensitive to the initial puff gas fill pressure (within limits of about a factor of 3). Spectroscopic studies of C and O impurity lines indicate that the density is sustained by recycling after the first 0.5 ms, with a magnitude determined by the applied RMF torque and plasma resistivity. The FRC can be sustained as long as the RMF is applied, and the 10 ms experimental sustainment time is about 50 times the natural flux confinement time of ∼200 μs, as determined by the external and internal field decay rates when the RMF is turned off.

The data shown in this paper were obtained using 1 m long strip antennae rather than the original 1.6 m long low inductance tube antennae, although the FRC length only decreased from about 1.8 to 1.6 m. This did, however, result in generally deeper penetration profiles due to the need to drive more current per unit antenna length [7] (it is a feature of RMF current drive that this penetration adjustment occurs naturally). The RMF was run at a frequency of $f_\omega = 105$ kHz. In the discharge shown in figure 1 there is an initial startup phase, lasting about 0.5 ms, where a relatively higher value of B_e is obtained. (B_e is measured by an external probe located outside the plasma tube, just under a central copper flux ring, and approximately equals $B_z(r = 40\,\text{cm})$ measured with the internal probe during most of the discharge.) This peak field can be up to 50% higher than during the following period, which is attributed to an initially higher plasma temperature. The temperature is subsequently reduced by recycling impurity ingestion and strong radiation. After startup, the FRC settles into a phase we now call 'lower performance'. However, after about 4 ms B_{ext} and B_{int} begin to vary in an oscillatory manner, and then settle into a 'higher performance' mode after 5–6 ms. This higher performance mode is always accompanied by the generation of a steady toroidal field of about 1–2 mT near the FRC field null (which is usually a precursor to the first jump in B_e). The behaviour is highly repeatable, although the exact timing and number of transitions can vary somewhat from shot to shot. The average resistivity inferred from achieved densities and external fields will be shown to be up to a factor of two lower during the higher performance mode.

B_ω, and the resultant external field and FRC separatrix radius, decrease during the discharge, primarily due to multi-MW losses in the drive tubes of the RMF power supply. There is also some decay due to the 1.5–0.5 MW absorbed by the FRC during the pulse, as seen by the differences between the plasma and vacuum traces of B_ω in figure 1. After the first 0.5 ms, bolometric measurements show that a large fraction of the absorbed power is radiated away, which limits the plasma total temperature to 20–40 eV. The peak plasma density decays from about 2×10^{19} to 1×10^{19} m^{-3} during the discharge, roughly proportional to the decay in B_ω. It is seen, however, that the ratio B_e/B_ω increases, which is an unambiguous indication of higher performance.

3. Analysis

The azimuthal RMF force on the electrons $\langle j_{ez} B_r \rangle$ is due to the RMF induced in-phase axial oscillation of the electrons interacting with the radial component of the RMF. This translates into an applied torque equal to

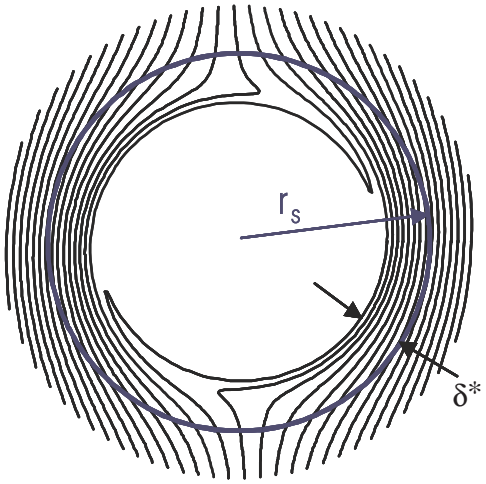

Figure 2. RMF lines calculated using the two-dimensional model of [4] for conditions where only partial penetration will occur. Partial penetration is the steady equilibrium solution for our experimental conditions where the average diamagnetic electron rotational frequency is less than the RMF frequency (see [2]).

$$T_{RMF} = \frac{2\pi r_s \delta^* B_\omega^2}{\mu_0} \ell_a, \tag{2}$$

where δ^* is the RMF penetration distance. Equation (2) is derived from the analytic solution of the RMF diffusion equation [2], and examination of the RMF internal structure in figure 2 gives an intuitive idea of why it scales in such a manner. We analyse the current drive in terms of torques since the RMF forces can be transferred to the FRC interior by various mechanisms, and must balance the total resistive retarding torque on the electrons. In the past, analytical expressions have been used for the RMF penetration distance δ^* ($\delta^* \sim (2\eta/\mu_0\varpi)^{1/2}$, with $\varpi = \omega - \omega_e$), but these are inappropriate for a plasma with non-uniform resistivity and electron rotation velocity. We will use actual measured values of δ^*, along with equation (2), in our data reduction analysis. Although equation (2) was derived from a uniform resistivity analysis, numerical calculations using the code described in [4] and [9], with non-uniform resistivity, show that this gives reasonable values for T_{RMF} even with non-uniform resistivity.

As a first step, we analyse experimental results for the retarding torque on the electrons based on a simple RR profile, with $B_z(r) = B_e \tanh K_{RR} u$, $n_e(r) = n_m \operatorname{sech}^2 K_{RR} u$ and $u = (r/R)^2 - 1$, where $R = r_s/\sqrt{2}$ is the location of the field null for an elongated FRC [12]. K_{RR} is a form factor near unity. Assuming a uniform resistivity $\eta_{RR} = m_e \nu_{ei}/e^2 n_e$, the torque on the electrons is then

$$\begin{aligned} T_{\eta RR} &= \int_0^{r_s} 2\pi(\omega_e - \omega_i) m_e n_e \nu_{ei} r^3 \, dr l_s \\ &= 0.5\pi e^2 n_m^2 \tanh K_{RR} (1 - \tfrac{1}{3} \tanh^2 K_{RR}) \\ &\quad \times (\omega_e - \omega_i) r_s^4 \eta_{RR} l_s / K_{RR}. \end{aligned} \tag{3}$$

We have included the ion rotation speed $\omega_i = 2\pi f_i$ since RMF driven FRCs in TCS are observed to spin up to about $f_i \sim 9$ kHz in the driven electron direction. Writing

$\omega_{RR} = \omega_e - \omega_i$, the peak value of the external field is $B_e = \mu_0 e n_m \omega_{RR} r_s^2/4K_{RR}$, and the torque can be expressed in terms of the external magnetic field, which is the most accurately measured quantity.

$$T_{\eta RR} = 2\pi e n_m \tanh K_{RR}\left(1 - \frac{1}{3}\tanh^2 K_{RR}\right) r_s^2 \eta_{RR} l_s \left(\frac{B_e}{\mu_0}\right). \quad (4)$$

Equating equations (2) and (4) yields a RR value for the average plasma resistivity:

$$\eta_{RR} = \frac{B_\omega^2(\delta^*/r_s)\ell_a/l_s}{e n_m \tanh K_{RR}(1-(1/3)\tanh^2 K_{RR})B_e} = \frac{1020 B_\omega^2(\mathrm{mT})(\delta^*/r_s)\ell_a/l_s}{n_m(10^{19}\mathrm{m}^{-3})B_e(\mathrm{mT})}\mu\Omega\,\mathrm{m}, \quad (5)$$

where we have taken $K_{RR} = 1$, which is an appropriate fit for the measured profiles. The RR profile has an edge value $B_z(r_s) = B_e \tanh K_{RR}$ and the above analysis does not take into account the resistive torque exerted by the edge plasma, where B_z increases to B_e and n_e drops from $n_m \operatorname{sech}^2 K_{RR}$ to zero.

If we calculate the resistivity based on the measured absorbed power, as has been done in the past [5, 6], the ratio of resistivity measured in this way, to that of equation (5), is given by $P_{abs}/(\omega_e T_{\eta RR})$ (we use ω_e rather than ω_{RR} for power calculations since the RMF force acts on the electrons). This ratio always considerably exceeds unity, which implies that the resistivity cannot be uniform. The recent numerical calculations of [9] show that the resistivity must be much higher in the edge region than in the centre in order to account for many of the observed data. We have thus developed a DRR model, with an interior rotation speed difference between ions and electrons of ω_{ri}, and an edge rotation difference $\omega_{re} = \omega - \omega_i$. The ion rotation is assumed to be uniform, consistent with Doppler broadening measurements [5]. We assume the inner region, with $u = (r/R)^2 - 1$, extends out to a location $u^* < 1$. In the outer region we modify the simple RR profile by defining a variable $w = (r/R_e)^2 - 1$ so that $B_z(r) = B_e \tanh K_i u$, $n_e = n_m \operatorname{sech}^2 K_i u$ for $u \leqslant u^*$ and $B_z(r) = B_e \tanh K_e w$, $n_e = n_m \operatorname{sech}^2 K_e w$ for $u \geqslant u^*$. The values of u^* and ω_{ri}, are determined from requiring the DRR profile to have the same $\langle\beta\rangle$ as measured from internal probes, and making it produce the measured B_e. For a given value of K_i for the inner region, the edge region parameters R_e and K_e can be determined by matching n_e and B_z at $r^* = R(1+u^*)^{1/2} = R_e(1+w^*)^{1/2}$. The solutions can be obtained from graphical plots of u^* versus $\langle\beta\rangle$ for K_i chosen to best match the actual profile. We use $K_i = 1$, but the final results have very little dependence on this choice. u^* always turns out to be between 0.6 and 0.85, corresponding to r^* between $1.27R$ and $1.36R$, very close to the separatrix at $r_s = 1.41R$. Equilibrium constraints thus result in a very narrow edge region where the density decreases to near zero, in agreement with observations for our RMF driven FRCs. This contrasts with the simple $K_{RR} = 1$ RR value of $n_e(r_s)/n_m = \operatorname{sech}^2 1 = 0.42$.

A comparison of the density profile obtained from internal field measurements (described in section 4) and that of the DRR model is shown in figure 3. The experimental profile was calculated from one-dimensional radial pressure balance, using both the measured B_z and B_θ fields and the interferometric line density, assuming a constant total temperature (calculated as 22 eV). The DRR profile has $K_i = 1.0$ and $K_e = 7.2$, which brings the separatrix density down to a low value matching the experimental measurements. A continuation of the $K_i = 1$ simple RR profile is indicated by the dashed lines. The inner difference between electron and ion rotation frequencies of $\omega_{ri} = 0.127 \times 10^6$ rad s^{-1} is slightly under the simple RR value of $\omega_{RR} = 0.143 \times 10^6$ rad s^{-1}. The agreement between the experimental and RR profiles is sufficient for our simple modelling, representing the strong edge effects produced by the RMF drive.

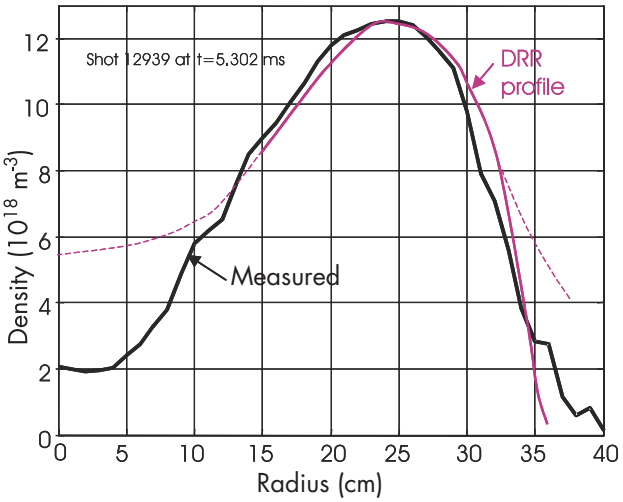

Figure 3. Comparison of the measured density profile, as obtained from internal field measurements, with that of the DRR model. DRR model conditions are $r_s = 36$ cm, $R = 25.5$ cm, $K_i = 1$, $u^* = 0.65$ ($r^* = 32.8$ cm), $R_e = 31.3$ cm, $K_e = 7.17$, $\omega_{ri} = 0.127 \times 10^6$ rad s^{-1}, and $\omega_{re} = 0.6 \times 10^6$ rad s^{-1}.

Calling η_i and η_e the resistivities in the inner and edge regions, respectively, the torque calculated from the DRR model is

$$T_{\eta DRR} = 2\pi e^2\left\{\eta_i\omega_{ri}\int_0^{r^*} n^2(r) r^3\,\mathrm{d}r + \eta_e\omega_{re}\int_{r^*}^{r_s} n^2(r) r^3\,\mathrm{d}r\right\} l_s = \pi e^2\left\{\eta_i\omega_{ri}R^4\int_{-1}^{u^*} n^2(u)(1+u)\,\mathrm{d}u + \eta_e\omega_{re}R_e^4\int_{w^*}^{w_f} n^2(w)(1+w)\,\mathrm{d}w\right\} l_s, \quad (6)$$

where $w_f = (r_s/R_e)^2 - 1$. Ignoring the inconsequential torque between $r = 0$ and $r = R(1-u^*)^{1/2}$ in the first integral, and using an average value of $w_a = (w^* + w_f)/2$ in the $(1+w)$ term in the second, a simple analytic expression can be arrived at. Writing $F(x) = \tanh x(1-(\tanh^2 x)/3)$, and using the matching result that $R_e = (\omega_{ri}K_e/\omega_{re}K_i)^{1/2}R$ and $R = r_s/\sqrt{2}$, this is

$$T_{\eta DRR} = 0.5\pi e^2 n_m^2 \omega_{ri} r_s^4 \frac{F(K_i u^*)}{K_i} \times\left\{\eta_i + \frac{\omega_{ri}K_e}{\omega_{re}K_i}\left(\frac{1+w_a}{2}\right)\left(\frac{F(K_e w_f)}{F(K_i u^*)} - 1\right)\eta_e\right\} l_s. \quad (7)$$

K_e is always fairly large (to bring the separatrix density down to near zero), and the parameter $(\omega_{ri}K_e/\omega_{re}K_i)$ is generally about 1.5. $R_e w_f$, which gives the separatrix conditions, is always between 1.5 and 2.5. If we divide the torque into inner

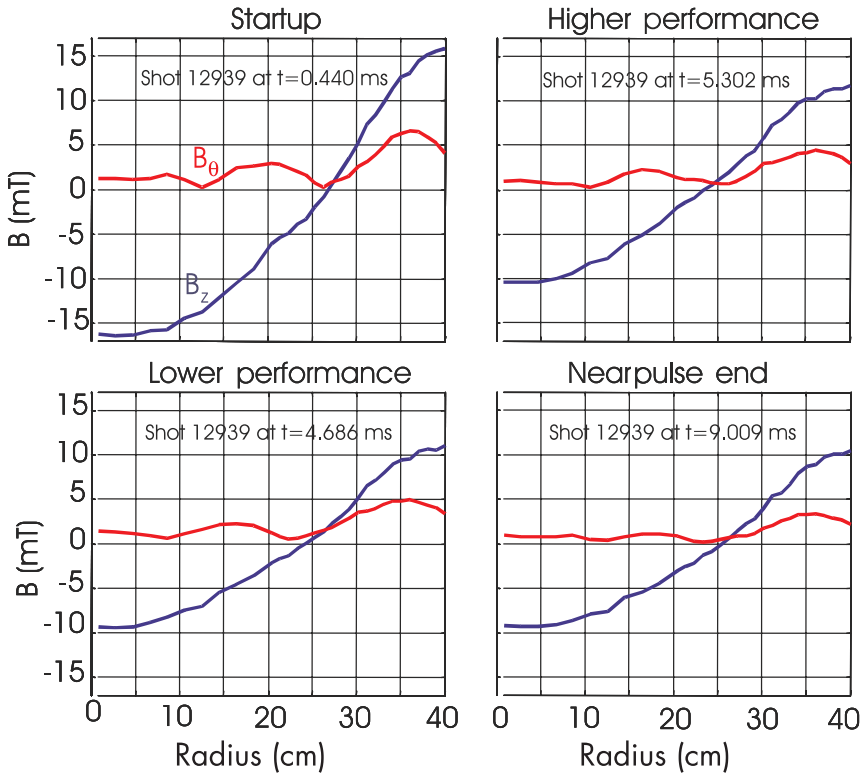

Figure 4. Profile measurements for discharge 12939 at various times. Internal probe at 45° to axis; application of 10 kHz low pass filter called B_z and portion at 105 kHz called B_θ.

and outer contributions, $T_{\eta i}$ and $T_{\eta e}$, the absorbed power is given by

$$P_{abs\theta} = (\omega_{ri} + \omega_i)T_{\eta i} + \omega T_{\eta e}. \quad (8)$$

Equating equation (7) to equation (2) and equation (8) to the measured absorbed power, gives us simultaneous equations for the inner and outer resistivities. We have used $P_{abs\theta}$ to represent the portion of absorbed power attributable to the azimuthal currents, and the largest source of error in the analysis lies in choosing this fraction. We use $P_{abs\theta} = P_{abs}/(1 + (B_\omega/B_e)^2)$, which is fairly arbitrary, but choosing the full measured P_{abs} in equation (8) sometimes yields negative values of η_i, and reducing $P_{abs\theta}$ further (by say $1 + (r_s/\delta^*)(B_\omega/B_e)^2$) sometimes gives unrealistic results with η_e less than the average value. In the data reduction we will use these two limits to place error bars on the calculations of η_i.

4. Resistivity measurements

Profile data for both the poloidal field $B_z(r)$ and the envelope of the RMF component $B_\theta(r)$ were obtained with a 6 mm diameter boron-nitride covered internal probe inserted from the top of TCS down to the centreline. The probe contained 31 single axis multi-turn loops spaced every 2 cm for the first 20 cm, and then every 1 cm out to the edge of the plasma tube. The probe could be oriented to record the axial field B_z, the horizontal field B_x, or a combination of the two. Usually, the probe was oriented at 45° to the plasma tube centreline to equally record B_z and B_x. The component at the 105 kHz RMF frequency was then assumed to be due to the RMF B_θ, and the remainder to represent B_z. Assuming all the steady components to be due to the axial field alone will be seen to be not strictly correct, but pure B_z measurements show the errors are small.

The profiles of $B_z(r)$ and $B_\theta(r)$ obtained in the above manner are shown in figure 4 for four times in a particular discharge. On careful examination, there is a subtle but distinct and highly repeatable difference in the B_θ profiles during the lower and higher performance phases. During the lower performance phase, the minimum in B_θ occurs inside the field null. This is as would be expected from simple, uniform resistivity calculations. Based on two-dimensional (r, θ) calculations it is not understood why the 105 kHz signal increases inside the field null, but it is probably due to three-dimensional effects, since axial oscillatory currents on outer field lines should be reflected by similar currents on their inner field line connections. During the higher performance phase the minimum in the B_θ profile occurs well outside the FRC field null. This is seen to produce a relatively higher value of the external field, and the drive performance, as characterized by the ratio of B_e/B_ω, improves.

Resistivities inferred from the simple RR calculations and from the DRR model for the four times shown in figure 4 are listed in table 1, along with data from lower (red entries) and higher performance modes for two other discharges. The values of δ^*/r_s are taken from the $B_\theta(r)$ traces based on the position where B_θ decreases to one-half its peak value. Since the inferred resistivity is linearly dependent on this value, there is some room for error, but the maximum possible RMF torque given by analytic calculations [2] corresponds to an effective value of $\delta^*/r_s = 0.38$, and the procedure is reasonable. The listed value for η_{RR} is given by equation (5).

Table 1. Resistivities inferred from the DRR model.

Shot	θ^*/r_s	n_m (10^{19} m^{-3})	η_{RR} ($\mu\Omega$ m)	η_{pabs} ($\mu\Omega$ m)	η_{inner} ($\mu\Omega$ m)	η_{edge} ($\mu\Omega$ m)
12939						
0.4 ms	0.16	1.70	109	260	30	380
4.7 ms	0.21	1.05	209	432	95	650
5.3 ms	0.185	1.26	124	393	3	590
9.3 ms	0.195	1.21	97	347	1	500
12889						
6.3 ms	0.23	0.95	269	425	204	480
7.0 ms	0.18	1.10	136	345	28	660
12951						
4.2 ms	0.21	1.12	212	404	127	610
5.0 ms	0.18	1.38	114	349	3	580

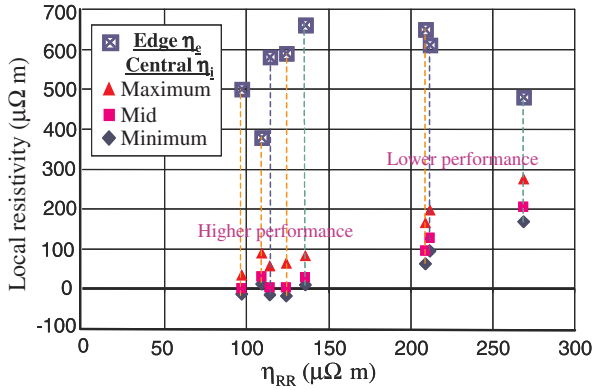

Figure 5. Inner and edge FRC resistivities based on the DRR model.

B_ω and B_e are measured accurately, but our cross-tube CO_2 interferometer is only valid for the first 2 ms due to vibrations, and the line density values for later times are scaled from cross-tube continuum radiation measurements. The peak density is calculated from the pressure profile, including contributions from both the ion centrifugal force and the RMF $\langle j_z B_\theta \rangle$ radial force, assuming the total temperature is uniform. This procedure should be reasonably accurate, even after the formation phase, since the density does not vary much and Langmuir probe measurements show the electron temperature to be uniform to $\pm 10\%$. It should be noted that n_m, along with B_e, increases during the transition from the lower to the higher performance mode.

The values of η_{pabs} in table 1 are given by the RR formula $(P_{abs\theta}/\omega_e T_{RMF})\eta_{RR}$, where ω_e is taken as $\zeta\omega + (1-\zeta)\omega_i$. ζ is determined from internal probe measurements and the measured line density, and is between 0.29 and 0.35 for all conditions except the 9.3 ms entry, where it is 0.24. It can be seen that η_{pabs} always exceeds η_{RR} by at least a factor of two, which we infer is attributable to a high edge resistivity, where most of the RMF power (always over 50%) is absorbed. The greater the difference, the greater will be the calculated difference between η_i and η_e in our DRR modelling. It can be seen that during the higher performance mode η_i is generally under 30 $\mu\Omega$ m. This value is reasonable given the relatively high ratios v_{De}/v_{ti} of electron drift velocity to ion thermal speed ($v_{De} = \omega_{ri} r \sim 5 \times 10^4$ m s^{-1} near the field null and 2×10^5 m s^{-1} near the edge, with $v_{ti} \sim 3 \times 10^4$ m s^{-1} everywhere), which tend to lead to drift wave micro-turbulence. The much higher ratios of v_{De}/v_{ti} in the outer edge, along with any RMF induced turbulence, would be expected to result in much higher resistivities there.

The inner and outer resistivities calculated using the DRR model are plotted in figure 5 versus the simple RR resistivity η_{RR}. Error bounds are shown on η_i based on the various assumptions mentioned earlier of how much of P_{abs} is assigned to $P_{abs\theta}$. The leftmost grouping corresponds to the higher performance mode, or to the startup condition for discharge 12939 (orange dashed lines). The blue diamonds are based on assuming $P_{abs\theta} = P_{abs}$, which clearly leads to non-physical negative values of η_i. The upper limit orange triangles are also somewhat non-physical since, in the lower performance cases they sometimes lead to values of η_e being less than η_i. Only the most likely value of edge resistivity is shown.

The lower inner resistivities during the higher performance phase could be the reason for the shallower RMF penetration. RMF penetration not reaching the field null was originally regarded as a mystery since in steady-state the azimuthal electric field

$$E_\theta = \eta_\perp j_\theta + v_{er} B_z - \langle v_{ez} B_r \rangle \tag{9}$$

must be zero everywhere. In uniform resistivity code calculations it was the RMF generated inward flow velocity that could distribute the RMF torque to the portion of the FRC where the RMF drive (bracketed term) did not penetrate (this is why we use a torque based analysis), but it was difficult to see how equilibrium could be achieved when at least some RMF did not penetrate to the position where $B_z = 0$. Later non-uniform resistivity calculations showed how the drive process could be intrinsically unsteady, with some inner RMF rotating at $f_{ri} + f_i$ and continually tearing and reconnecting with the outer RMF rotating at the full f_ω [9]. (The lower rotating component of B_θ would not be accounted for in plots such as those shown in figure 4 where only the 105 kHz component of the 45° aligned probes was assigned to B_θ.) This process with two distinct electron rotational speeds was termed 'edge driven' current drive. The non-steady behaviour produces a non-steady torque oscillating at $f_\omega - (f_{ri} + f_i)$, which causes the FRC flux and all $B_z(r)$ to oscillate at that frequency.

This 'edge driven mode' behaviour is clearly seen in the contour plots of the frequency content of the internal probe signals shown in figure 6, where the internal probe was oriented to see both B_z and B_x. The average difference between electron and ion rotation frequencies needed to produce the measured B_e based on the measured density profile is about 35 kHz for all the long pulse data. The calculated DRR central value of $f_{ri} = \omega_{ri}/2\pi$ is, of course less, about 25 kHz. The early time contour plot (*a*) shows a distinct frequency content peak at ~30 kHz (mostly in B_x as determined when the probe is oriented in the x direction), and again at sidebands of this frequency around the 105 kHz RMF frequency (mostly in B_z). (The ~70 kHz sideband can also be seen in the B_{ext} signal of figure 1, where a 10 kHz spike filter around 105 kHz has been applied to remove spurious RMF pickup.) The 30 kHz content is much lower after the higher performance phase begins, with the principal frequency content then occurring at about 18 kHz due to an $n = 2$ distortion developing and rotating at the ion rotation frequency of $f_i = 9$ kHz. The rotational $n = 2$ instability is ubiquitous, and usually lifetime limiting in standard theta-pinch formed FRCs, which spin up

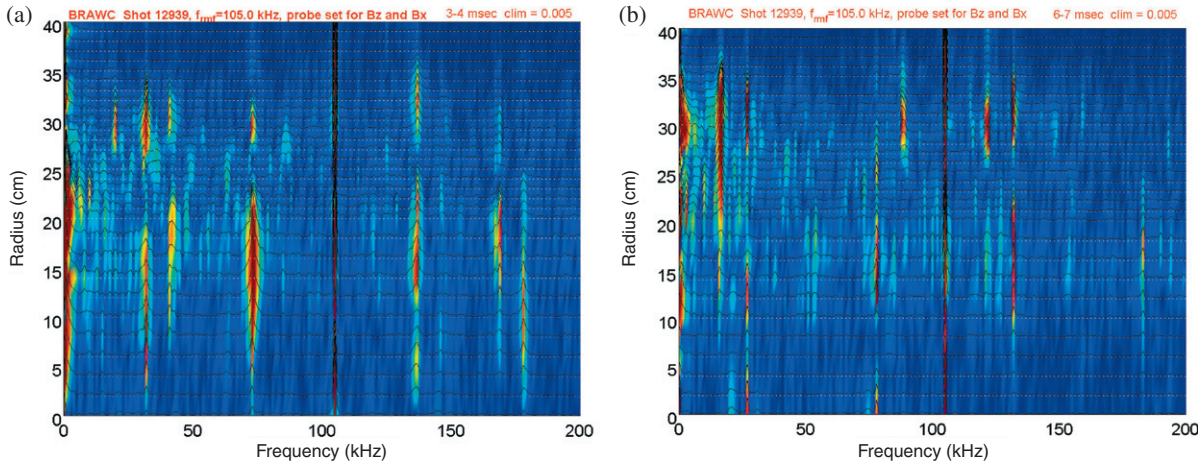

Figure 6. Internal probe frequency content for discharge 12939 with internal probe oriented to measure both B_z and B_x at (*a*) 3–4 ms and (*b*) 6–7 ms.

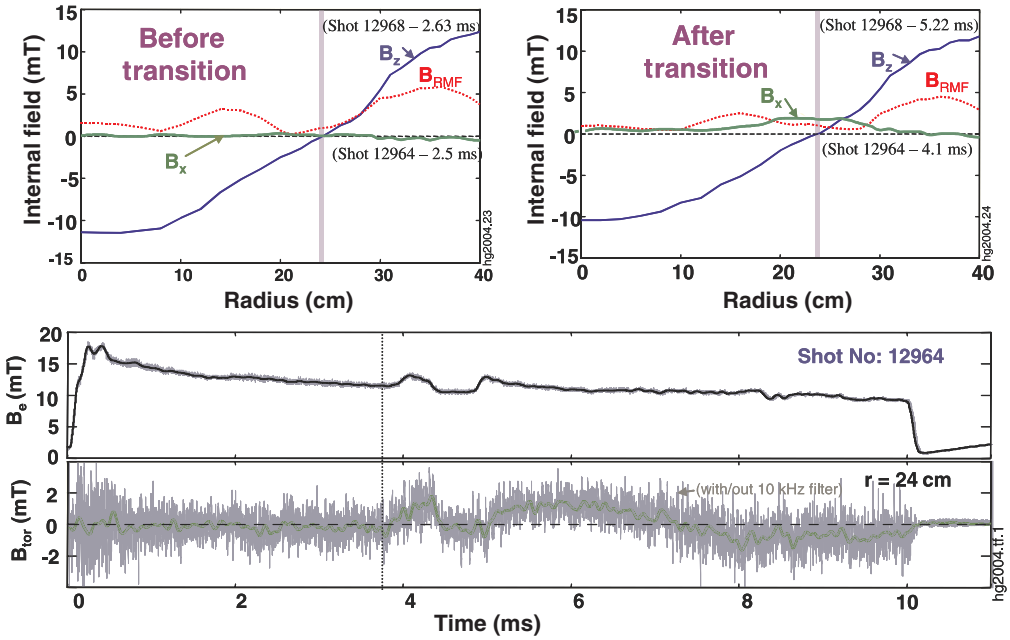

Figure 7. Toroidal field development during transition to higher performance mode. B_z and B_θ profiles taken with internal probe aligned at 45° to the z-axis. $B_{\rm tor}$ obtained with internal probe aligned to record only B_x.

in the ion diamagnetic direction. RMF sustained FRCs spin up in the electron direction, usually to a relatively higher velocity compared to the ion thermal velocity. The radial pressure imposed by B_ω has been measured to have a strong stabilizing effect on the rotating $n = 2$ instability [13], but the ion rotation frequency is almost independent of the magnitude of B_ω. It is thus not surprising that the $n = 2$ distortion develops as the RMF magnitude runs down.

A very interesting feature of the transition to the higher performance mode is the development of a steady toroidal field. This was measured on discharges where the internal probe was aligned to record only B_x, which is assumed to represent the toroidal field since the same phenomenon is seen on all such shots. The time trace in figure 7 shows the external field plus measured probe signal near the field null, both unfiltered and with a 10 kHz low-pass filter applied. The first transition to an increase in $B_{\rm e}$ seems to be preceded by the development of a weak toroidal field. Once the higher performance mode is fully established (after 5 ms for the discharge shown in figure 7) the toroidal field sometimes changes direction (as seen at 7 ms in figure 7), but this does not seem to affect the overall performance. Since we only measure the internal field at the FRC midplane, we cannot comment on its overall axial structure.

The toroidal field is too small to have much influence on the overall FRC equilibrium, but it can be large compared to the poloidal field near the field null, and may affect transport properties there. Detailed profiles are also shown in figure 7 for the toroidal field both before and after the transition to the higher performance mode. They are superimposed on B_z and B_θ profiles obtained on a different shot with the internal probe aligned in the normal 45° manner.

We are not certain what causes the transition to the higher performance mode, but we suspect it may be related to a decrease in the ratio of $B_\omega/B_{\rm e}$ as the RMF magnitude

decreases. This decrease occurs independent of the performance mode because B_e scales as $(n_e T_t)^{1/2}$, while n_e scales approximately linearly with B_ω and the total temperature tends to be rather independent of RMF magnitude. It also cannot be said at this time whether the toroidal field development leads to higher performance, or is just a consequence of it. However, calculations based on relaxation to high beta minimum energy states, with conservation of generalized helicity, generally yield small toroidal fields [14], and other measurements of translated FRCs in TCS also showed small toroidal fields [15], so we might be seeing additional evidence of such a relaxation process.

5. Summary and conclusions

It is possible to both form FRCs and sustain them for long periods in quasi-steady-state using RMFs. A much better understanding of the current drive process has been obtained through the use of detailed profile and frequency spectrum measurements coupled with numerical calculations. The RMF drive process appears to be characterized by strong drive in the edge region near the FRC separatrix, accompanied by fairly high plasma resistivity. The measured interior and edge values are fairly typical of Chodura type resistivity ($\eta \sim (1000/n_e^{1/2}(10^{19}\,\mathrm{m}^{-3}))[1 - \exp(v_{De}/f v_{ti})]\,\mu\Omega\,\mathrm{m}$ with $f \sim 3$), which was previously used to model FRC flux decay [16].

A higher performance mode appears to develop spontaneously for longer RMF pulse lengths, at least under the circumstances under which the TCS experiments were run. A trigger for this mode has not been identified, but it may be related to the aforementioned lower values of B_ω/B_e. The mode is accompanied by the spontaneous development of small values of the toroidal field, which could possibly signify a relaxation process. The net result appears to be fairly low interior plasma resistivities. Plasma turbulence is minimized when the RMF magnitude is small compared to the axial confinement field. These conditions were only achievable in TCS at low values of B_ω since the plasma temperature, which along with the plasma density sets the diamagnetic current in high beta FRCs, was held low by impurity radiation. Better performance at higher values of B_ω should be achievable if the impurity content can be lowered and temperatures raised.

The edge drive properties of RMF, along with the resultant high edge resistivity and high edge thermal deposition, may rule out RMF as a stand-alone FRC current drive mechanism. However, RMF can be extremely useful for startup, and has been seen to greatly enhance particle lifetimes [17] and interchange stability [13]. It should be ideally suited for use in conjunction with tangential neutral beam injection (TNBI) current drive near the field null, since the RMF torque, which leads to plasma rotation, could be balanced by TNBI momentum injection in the opposite direction. It may even be possible to influence the azimuthal current and velocity profiles, which could lead to controllable enhancement of performance rather than the spontaneous transitioning between performance modes seen in the pure RMF drive experiments. Monte Carlo TNBI calculations show that to effectively utilize TNBI the TCS flux levels will have to be raised from the present 2 mWb levels (when using the low inductance RMF antennae) to over 5 mWb [18]. This can be done if the plasma temperature can be increased to the 100 eV level. Modifications to minimize impurities, including changing to a mostly all metal construction (except for a single central 1.25 m long quartz section protected by internal metal flux rings) with larger inlet and output tubes, are currently underway. The entire vacuum system will be bakeable to 200°C and have provisions for discharge cleaning and wall conditioning.

Acknowledgments

The authors would like to thank the entire RPPL team for operating and maintaining TCS. The work was supported by the US Department of Energy.

References

[1] Jones I.R. and Hugrass W.N. 1981 Steady-state solutions for the penetration of a rotating magnetic field into a plasma column *J. Plasma Phys.* **26** 441
[2] Hoffman A.L. 2000 Rotating magnetic field current drive of FRCs subject to equilibrium constraints *Nucl. Fusion* **40** 1523
[3] Hugrass W.N. 1986 The influence of the spatial harmonics on the RMF current drive *Aust. J. Phys.* **39** 513
[4] Milroy R.D. 2000 An MHD model of RMF current drive in an FRC *Phys. Plasmas* **7** 4135
[5] Guo H.Y. *et al* 2002 Formation and steady-state maintenance of FRCs using RMF current drive *Phys. Plasmas* **9** 185
[6] Hoffman A.L., Guo H.Y., Milroy R.D. and Pietrzyk Z.A. 2003 Resistivity scaling of RMF current drive in FRCs *Nucl. Fusion* **43** 1091
[7] Guo H.Y. and Hoffman A.L. 2004 Sustainment of elongated FRCs with localized RMF current drive *Phys. Plasmas* **11** 1087
[8] Hoffman A.L. *et al* 2002 The TCS rotating magnetic field FRC current-drive experiment *Fusion Technol.* **41** 92
[9] Milroy R.D. and Miller K.E. 2004 Edge-driven RMF current drive of FRCs *Phys. Plasmas* **11** 633
[10] Jones I.R. 1999 A review of RMF current drive and the operation of the rotamak as a field-reversed configuration (rotamak-FRC) and a spherical tokamak (rotamak-ST) *Phys. Plasmas* **6** 1950
[11] Collins G.A., Durance G., Hogg G.R., Tendys J. and Watterson P.A. 1988 Small aspect ratio tokamak configurations generated by RMF drive *Nucl. Fusion* **28** 255
[12] Tuszewski M.1988 Field reversed configurations *Nucl. Fusion* **28** 2033
[13] Guo H.Y., Hoffman A.L., Milroy R.D. and Votroubek G.R. 2004 Stabilization of interchange modes by rotating magnetic fields *Phys. Rev. Lett* submitted
[14] Steinhauer L.C. and Ishida A. 1997 Relaxation of a two-specie magnetofluid *Phys. Rev. Lett.* **79** 3423
[15] Guo H.Y., Hoffman A.L., Miller K.E. and Steinhauer L.C. 2004 Flux conversion and evidence of relaxation in a high-β plasma formed by high-speed injection into a mirror confinement structure *Phys. Rev. Lett.* **92** 245001
[16] Milroy R.D. and Slough J.T. 1987 Poloidal flux loss and axial dynamics during the formation of a field-reversed configuration *Phys. Fluids* **30** 3566
[17] Slough J.T. and Miller K.E. 2000 Enhanced confinement and stability of an FRC with RMF current drive *Phys. Rev. Lett.* **85** 1444
[18] Lifschitz A.F., Farengo R. and Hoffman A.L. 2004 Calculations of TNBI current drive efficiency for present moderate flux FRCs *Nucl. Fusion* **44** 1015